Semiconducting Polymer Nanoprobes for In Vivo Imaging of Reactive Oxygen and Nitrogen Species

Technical Journal Club

Tiziana Sonati

16.12.14

Outline

- Background: Molecular imaging in drug development
- Methods:
  1. Imaging of H_2O_2 with chemiluminescent nanoprobes (CRET) (Lee et al. Nat. Mater. 2007)
  2. Near-infrared (IR) probe for ROS imaging based on differential reactivity of linked cyanine dyes (FRET-based) (Oushiki et al. JACS 2010)
- Application papers for detection of oxidative and nitrosative stress in-vivo:
  - Systemic bacterial infection (Pu et al. Angew. Chem. Int. Edn. Engl. 2013)
  - Liver drug-toxicity testing (Shuhendler et al. Nat biotec 2014)
- Outlook: Improved drug design to minimize the formation of radical metabolites

Molecular imaging in drug development

- Assessment of biological and biochemical processes in living subjects

- Earlier detection and characterization of disease, and evaluation of treatment

- Repetitive, non-invasive and uniform studies of the same living subject using identical or alternative biological imaging assays at different time points reducing the number of animals required and cost

Willmann et al. Nat. Rev. Drug Discov. 2008

Drug development process

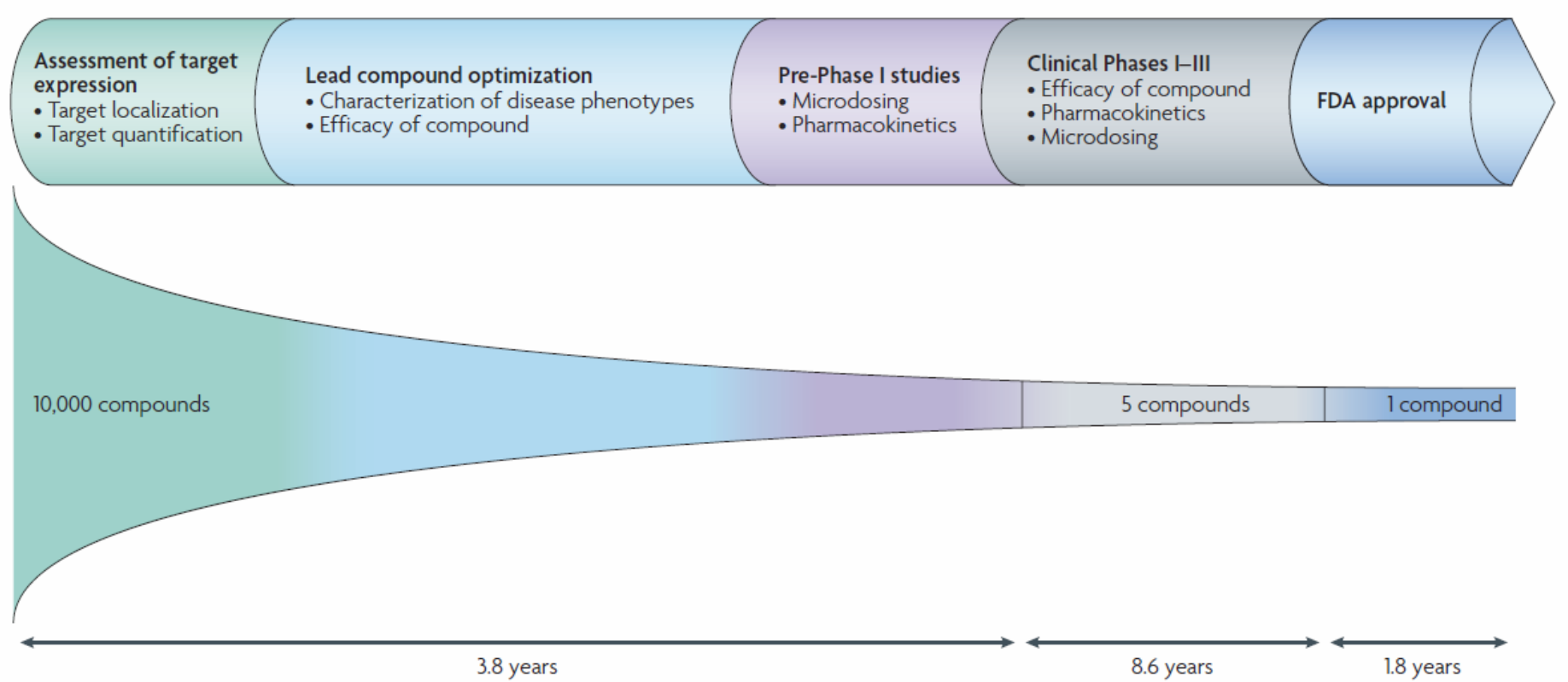

Figure 1 | **Molecular imaging and the drug development process.** On average, for ~10,000 compounds evaluated in preclinical studies, about five compounds enter clinical trials and about one compound finally receives regulatory approval by the US Food and Drug Administration (FDA)[3]. The mean time from synthesis of a new compound to marketing approval in the United States is 14.2 years[137]. Molecular imaging can be used at various stages in the drug development process, as illustrated here, which may help reduce attrition rates and allow the selection of the most promising drug candidates early on in development.

Willmann et al. Nat. Rev. Drug Discov. 2008

Toxicology profiling in discovery

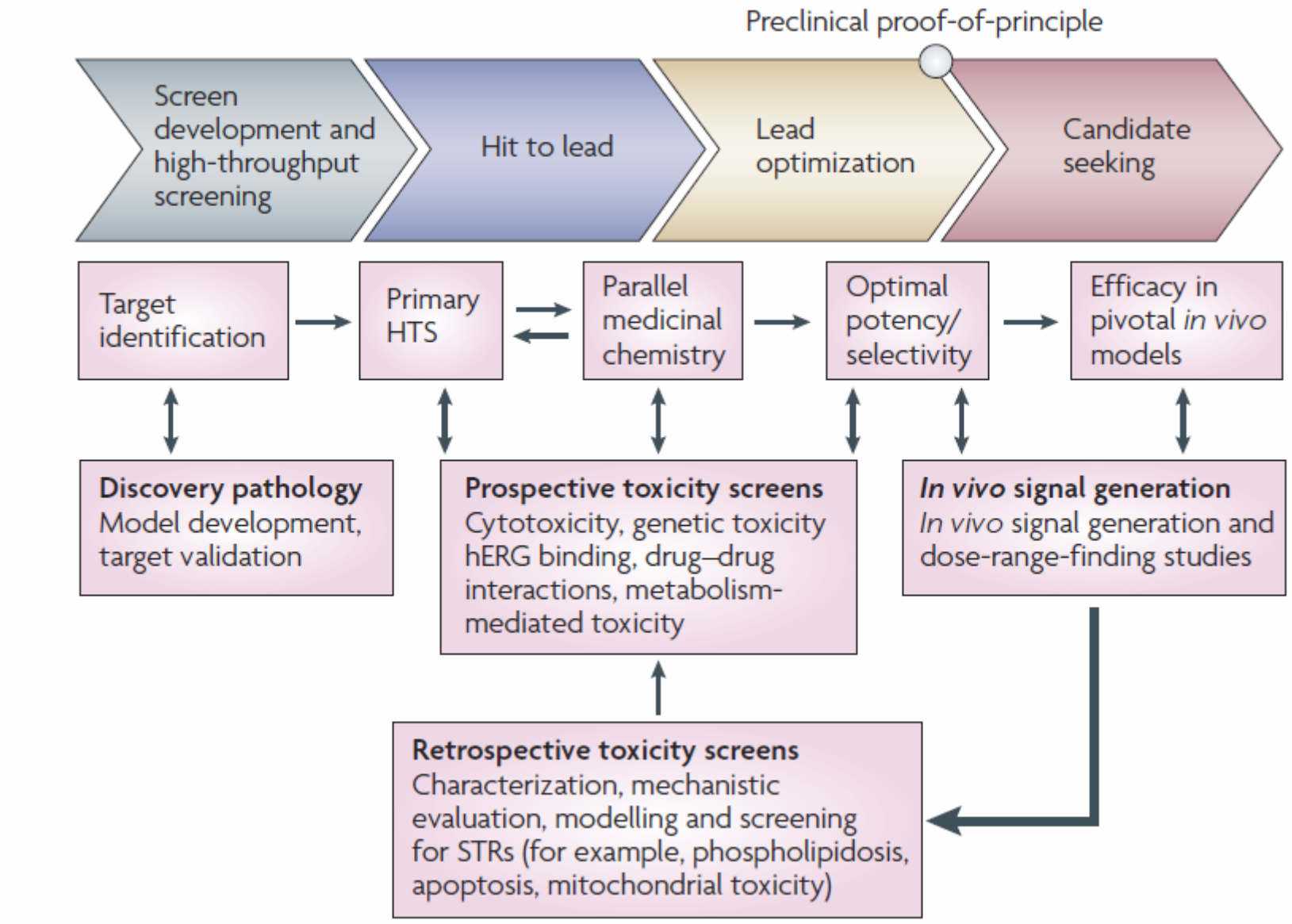

Methods for molecular imaging

Application tool to study toxicology in-vivo

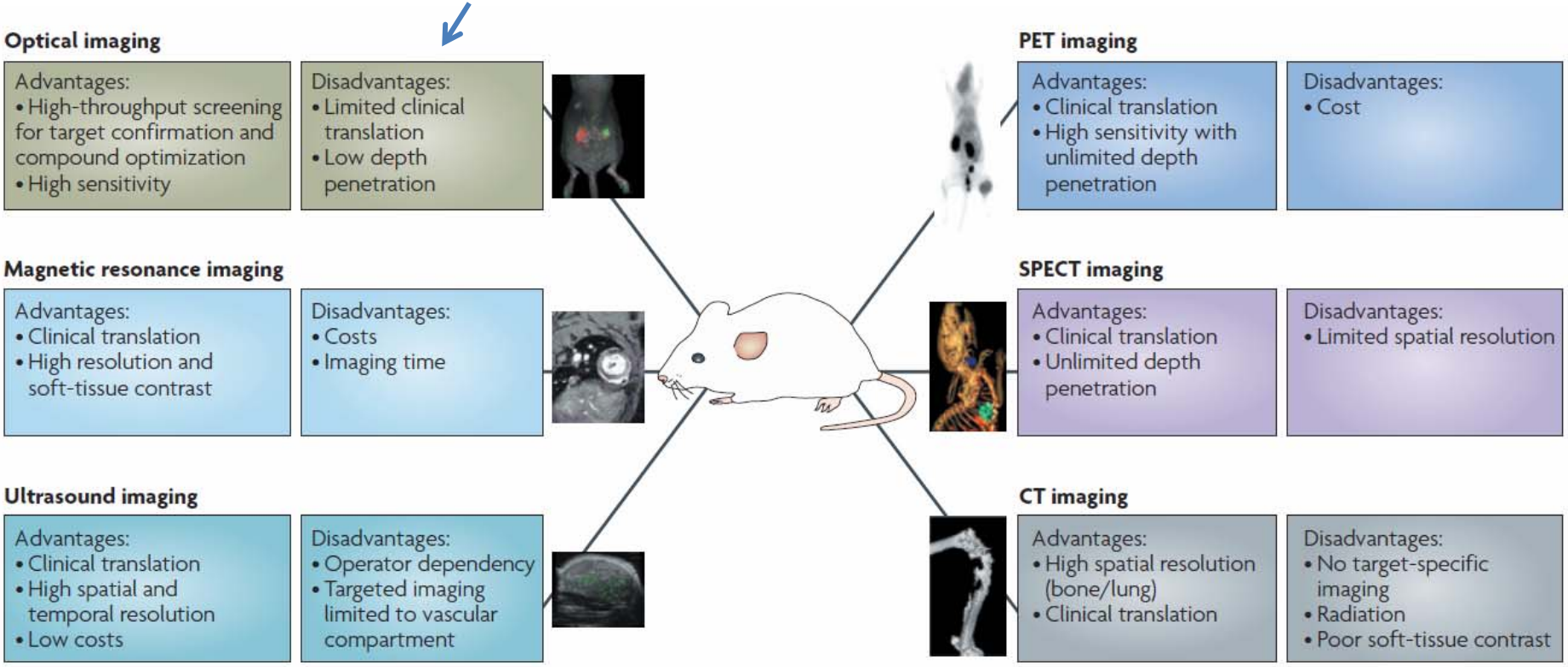

Figure 2 | **A summary of modalities used for molecular imaging.** Each modality has particular characteristics, advantages and limitations, which are highlighted here. Most imaging modalities are used clinically and can be translated from animals to humans in the drug development process. The different imaging modalities are generally considered complementary rather than competitive. See Supplementary information S1 (box) for a more detailed summary.
CT, computed tomography; PET, positron-emission tomography; SPECT, single-photon-emission computed tomography.

Willmann et al. Nat. Rev. Drug Discov. 2008

Importance of ROS imaging

Reactive oxygen species (ROS) operate as signaling molecules under various physiological conditions, and overproduction of ROS is involved in the pathogenesis of many diseases.

→Fluorescent probes for visualizing ROS are promising tools with which to uncover the molecular mechanisms of physiological and pathological processes and might also be useful for diagnosis.

1. Imaging of H_2O_2 with chemiluminescent nanoparticles (CRET)

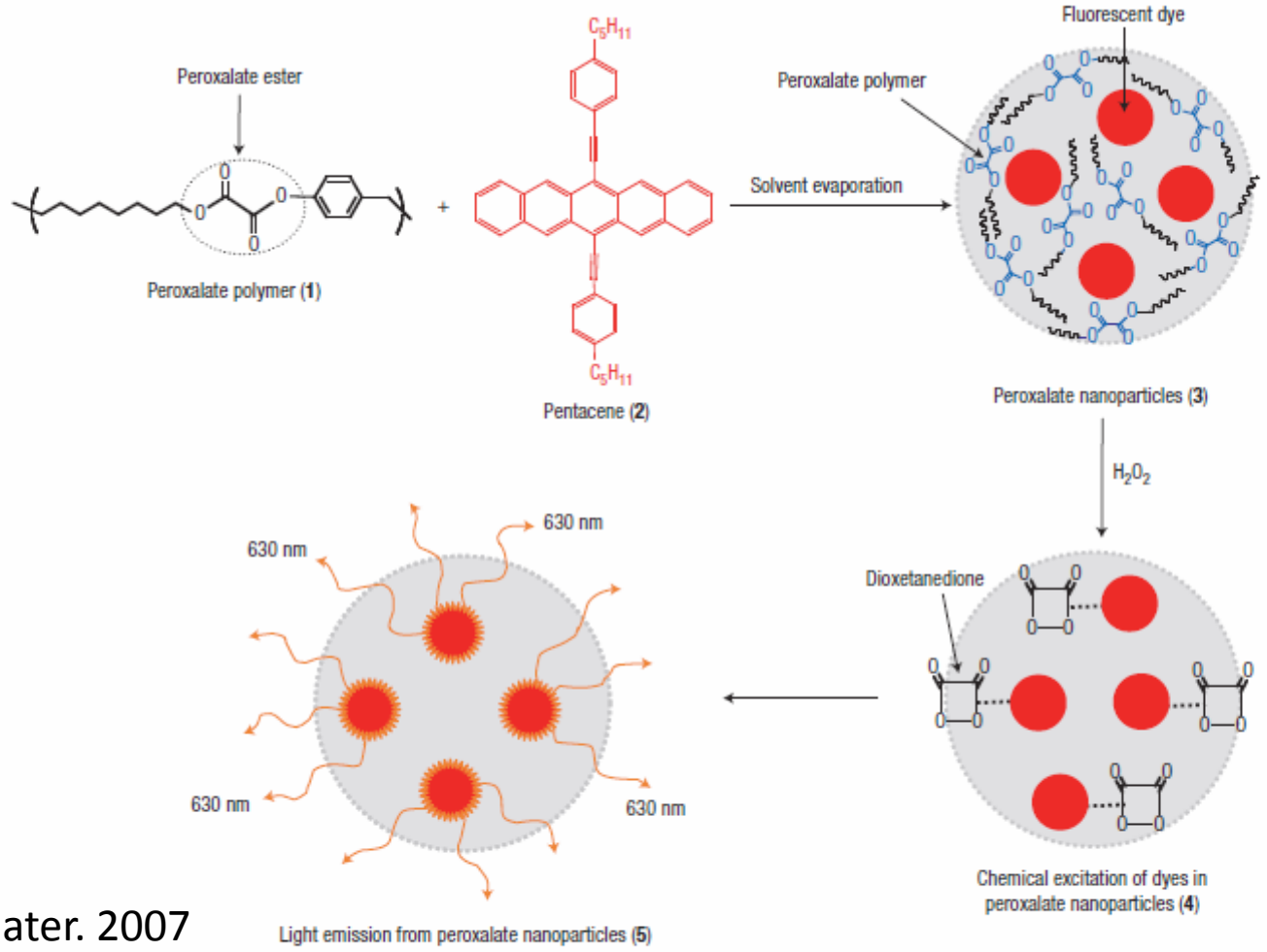

Lee et al. Nat. Mater. 2007

Figure 1 Peroxalate nanoparticles—a new strategy for imaging hydrogen peroxide *in vivo*. Peroxalate nanoparticles (**3**) are formulated from the peroxalate polymer (**1**) and a fluorescent dye (**2**), in this case pentacene. Hydrogen peroxide reacts with the peroxalate ester of **3** to produce a high-energy dioxetanedione intermediate within the nanoparticles (**4**), which then chemically excites the encapsulated dye, leading to light emission from the nanoparticles and the imaging of hydrogen peroxide (**5**).

1.Imaging of H_2O_2 with chemiluminescent nanoparticles (CRET)

Peroxalate nanoparticles properties:

- tunable wavelength emission (460–630 nm),
- nanomolar sensitivity
- excellent specificity for hydrogen peroxide over other reactive oxygen species
- dioxetanedione intermediate produced within the nanoparticles can chemically excite a variety of fluorescent dyes, including those in the near-infrared range (resulting in minimal absorption by haemoglobin, water and lipids)
- deep tissue-imaging capability

Lee et al. Nat. Mater. 2007

2. NIR probe for oxidative stress based on differential reactivity of linked cyanine dyes

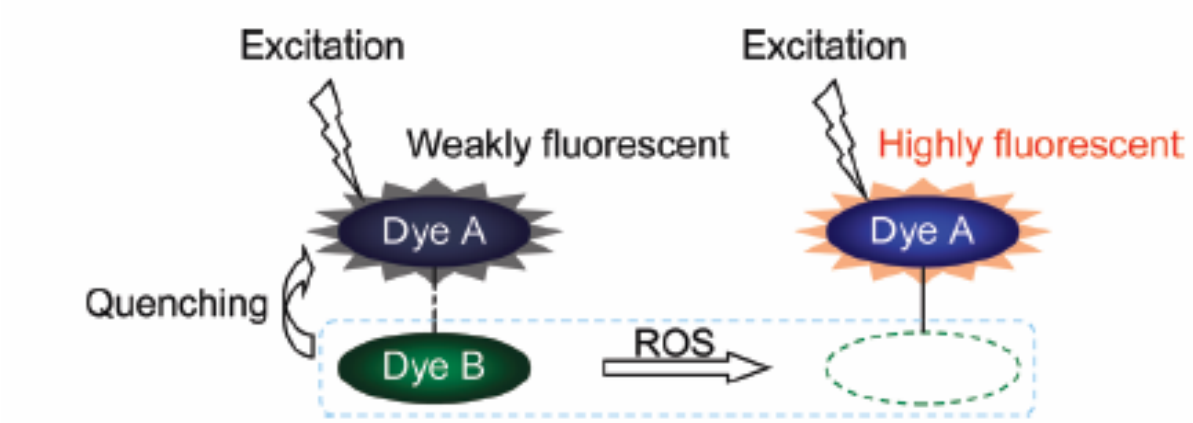

Figure 6. Design strategy utilizing two linked cyanine dyes.

Oushiki et al. JACS 2010

Angewandte International Edition Chemie

Biosensors

DOI: 10.1002/anie.201303420

Semiconducting Polymer Nanoprobe for In Vivo Imaging of Reactive Oxygen and Nitrogen Species**

*Kanyi Pu, Adam J. Shuhendler, and Jianghong Rao**

Goal: Develop and implement methods to detect radical species in an in-vivo model of LPS-induced inflammation

Method: dual-color semiconducting-polymer nanoparticle (SPN)-based near-infrared (NIR) nanoprobe for the detection of reactive oxygen and nitrogen species (RONS) (named, NanoDRONE)

Semiconducting polymer nanoparticles (SPNs)

- New class of photostable fluorescent nanomaterials with excellent brightness (orders of magnitude higher than that of small-molecule fluorophores, and tens of times better than that of QDs)

- Composed of p-conjugated polymers, their use as fluorescent probes eliminates the possibility of heavy metal ion-induced toxicity to living organisms → good biocompatibility

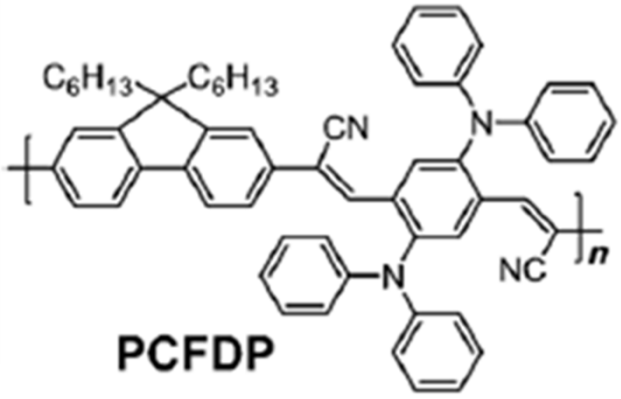

PCFDP

Preparation of the Nanoprobe

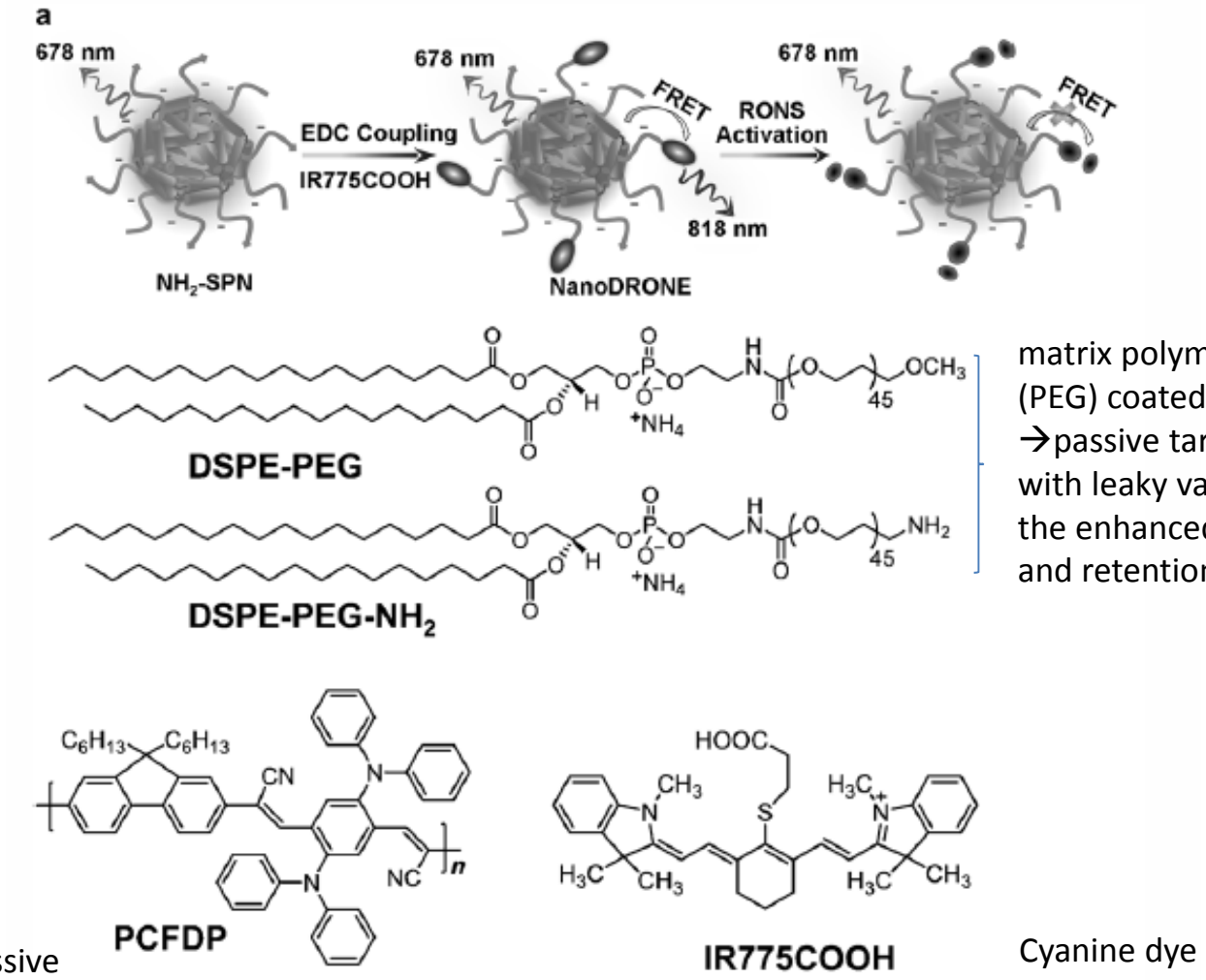

matrix polymers:
(PEG) coated nanoarchitecture
→passive targeting in tissues with leaky vasculature through the enhanced permeability and retention effect

NIR-emissive semiconducting polymer

Cyanine dye derivative undergoing oxidation-induced degradation in the presence of ROS and RNS

In-vitro characterization of Nanodrone

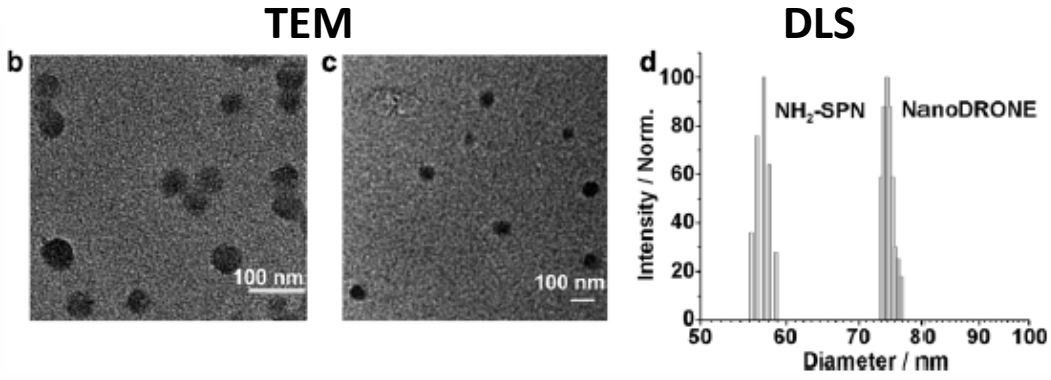

Resistant to RONS degradation

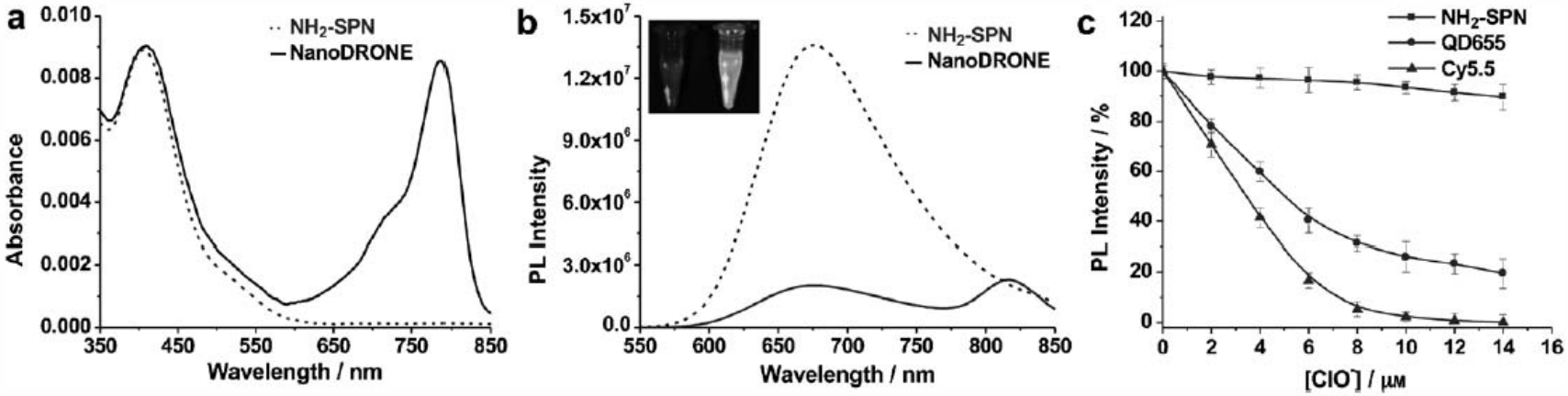

Figure 2. a) UV/Vis absorption and b) fluorescence spectra of NH_2-SPN and NanoDRONE in PBS (30 mM, pH 7.4). c) Fluorescence changes of NH_2-SPN, QD655, and Cy5.5 at 678, 655, and 693 nm, respectively, upon addition of ClO^- in PBS (30 mM, pH 7.4). [NH_2-SPN] = [Cy5.5] = 1.0 μg; [QD655] = 20 nM. Excitation wavelengths for NH_2-SPN, QD655, and Cy5.5 are 405, 500, and 630 nm, respectively. Error bars represent the standard deviation from three measurements.

Nanodrone specificity

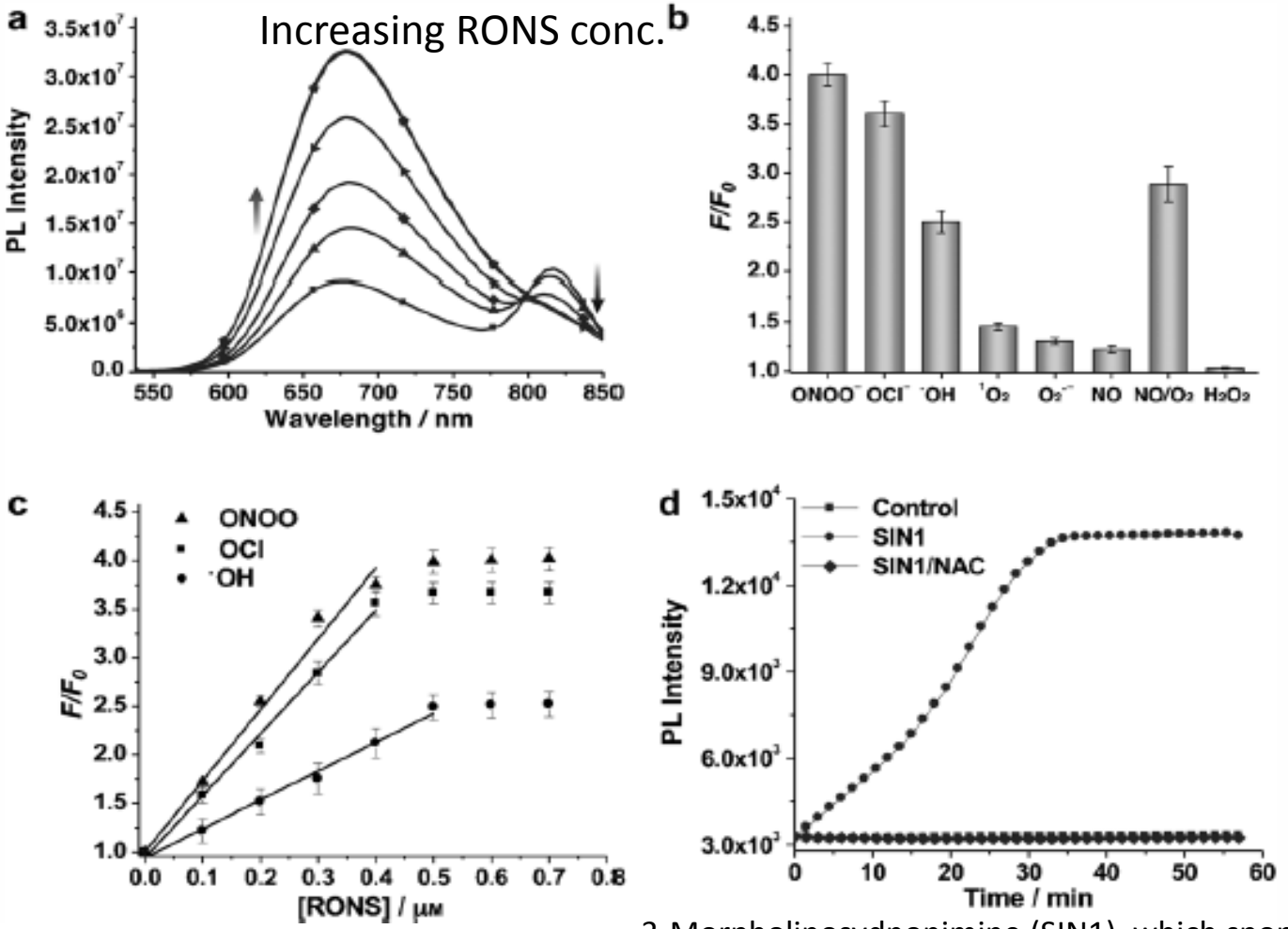

3-Morpholinosydnonimine (SIN1), which spontaneously releases NO and $O2^{\cdot-}$ to form ONOO in aqueous solution, was used to mimic the generation of ONOO by macrophages

Nanodrone to detect RONS in cells

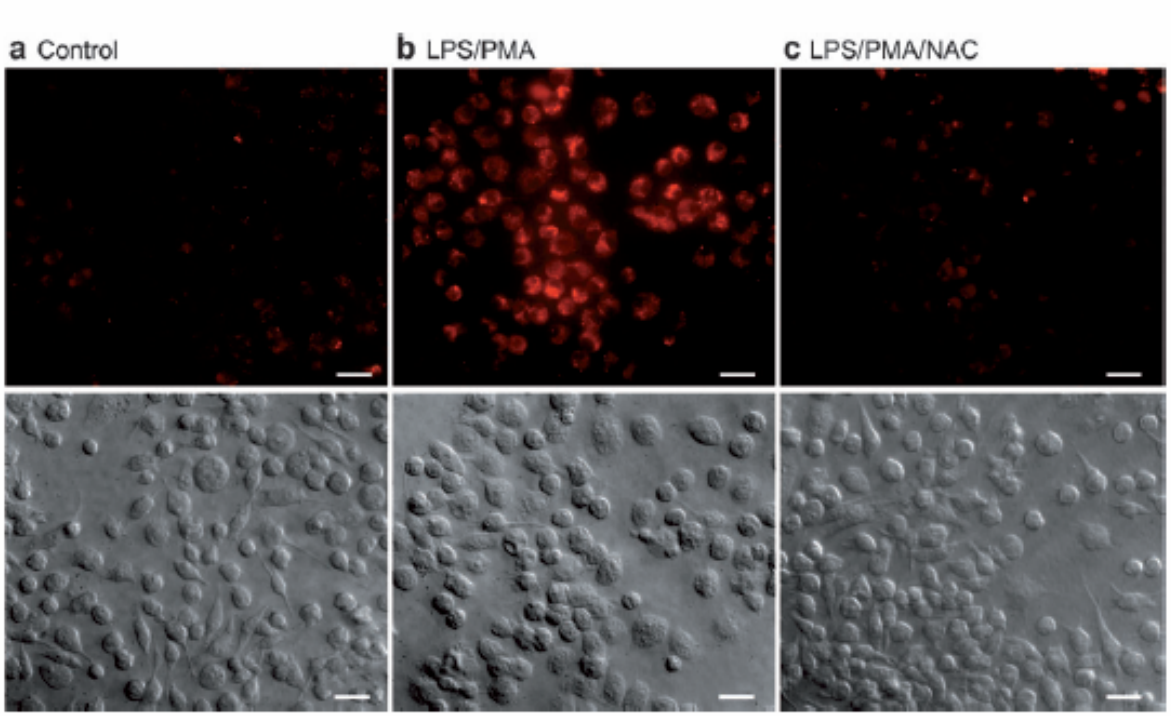

Figure 4. Fluorescence and differential interference contrast (DIC) images of live murine macrophages (RAW 264.7) incubated with NanoDRONE (1.5 $\mu g\,mL^{-1}$, 3 h) before imaging: a) nontreated cells, b) cells successively treated with LPS (2 h) and PMA (0.5 h), and c) cells pretreated with NAC 2 h before treated with LPS (2 h) and PMA (0.5 h), followed with NAC for 1 h. [LPS] = 1 $\mu g\,mL^{-1}$; [PMA] = 5 $\mu g\,mL^{-1}$; [NAC] = 1 mM. Scale bars: 20 μm.

Bacterial cell wall lipopolysaccharide (LPS) and phorbol 12-myristate 13-acetate (PMA) to elicit the elevated production of RONS such as ONOO and ClO

In vivo imaging of RONS with NanoDRONE in a LPS-induced acute peritonitis mouse model

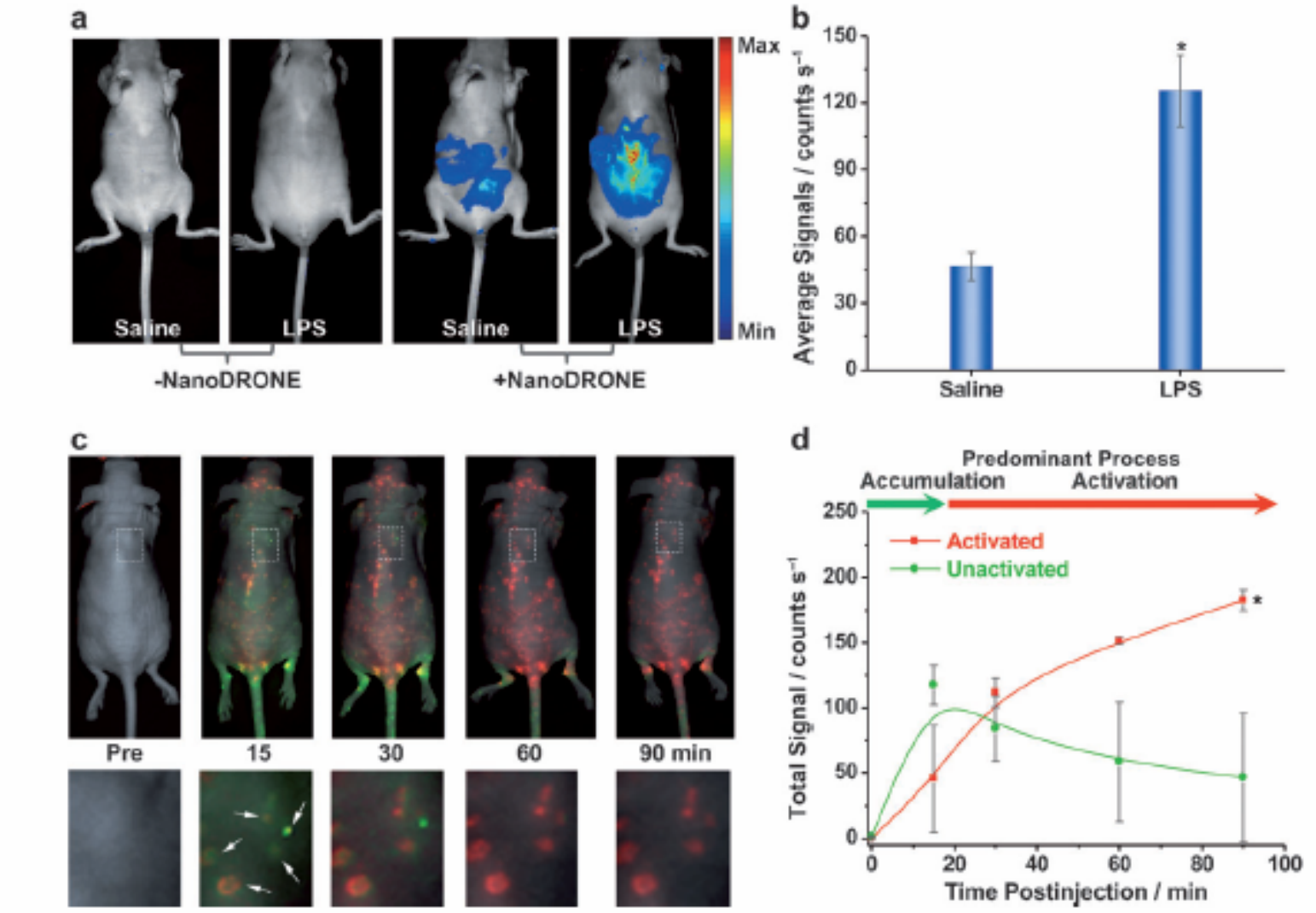

Summary

SPN-based NIR nanoprobe:

- combines RONS inert property of SPN with a RONS sensitive cyanine derivative for imaging of RONS
- presents high physiological stability, good biodistribution, long circulation half-life, and passive targeting to inflammatory regions

This nanoprobe allows for detection of RONS in the microenvironment of inflammation using systemic administration.

Disadvantage: the current probe does not show specificity over $ONOO^-$, ClO^-, $\cdot OH$ and, and is more suitable for detection of the RONS pool at inflammation sites in living animals.

nature biotechnology

Real-time imaging of oxidative and nitrosative stress in the liver of live animals for drug-toxicity testing

Adam J Shuhendler[1,3], Kanyi Pu[1,3], Lina Cui[1], Jack P Uetrecht[2] & Jianghong Rao[1]

Current drug-safety assays for hepatotoxicity rely on biomarkers with low predictive power. The production of radical species, specifically reactive oxygen species (ROS) and reactive nitrogen species (RNS), has been proposed as an early unifying event linking the bioactivation of drugs to hepatotoxicity and as a more direct and mechanistic indicator of hepatotoxic potential. Here we present a nanosensor for rapid, real-time *in vivo* imaging of drug-induced ROS and RNS for direct evaluation of acute hepatotoxicity. By combining fluorescence resonance energy transfer (FRET) and chemiluminescence resonance energy transfer (CRET), our semiconducting polymer–based nanosensor simultaneously and differentially detects RNS and ROS using two optically independent channels. We imaged drug-induced hepatotoxicity and its remediation longitudinally in mice after systemic challenge with acetaminophen or isoniazid. We detected dose-dependent ROS and RNS activity in the liver within minutes of drug challenge, which preceded histological changes, protein nitration and DNA double-strand-break induction.

Background

- Drug-induced hepatotoxicity is also the single most important cause of both US Food and Drug Administration (FDA) non-approval of drugs and withdrawal of drugs from the market after approval → innovative preclinical hepatotoxicity screening methods to reduce hepatotoxicity during drug development
- In the liver, drugs undergo enzymatic biotransformation, which enhances metabolite hydrophilicity and clearance from the body. However, biotransformation can also generate reactive radicals or reactive electrophiles through one- or two-electron oxidation reactions

Goal: Develop and implement methods to detect radical species (ROS, RNS) for preclinical drug-safety screening (direct evaluation of acute hepatotoxicity)

Method: nanosensor for rapid, simultaneous and differential detection of RNS and ROS using two optically independent channels by combining fluorescence resonance energy transfer (FRET) and chemiluminescence resonance energy transfer (CRET)

→ CF-SPN (CRET-FRET semiconducting polymer nanoparticles)

ROS, RNS and cellular mechanisms

ROS, including H_2O_2, can be generated:

- directly by oxidative phase I enzymes (for example, cytochrome P450 and peroxidase) during metabolism
- indirectly by the reaction of radical drug metabolites with oxygen

RNS such as peroxynitrite ($ONOO^-$) result from:

- drug metabolite-induced mitochondrial toxicity caused by disruption of the electron transport chain

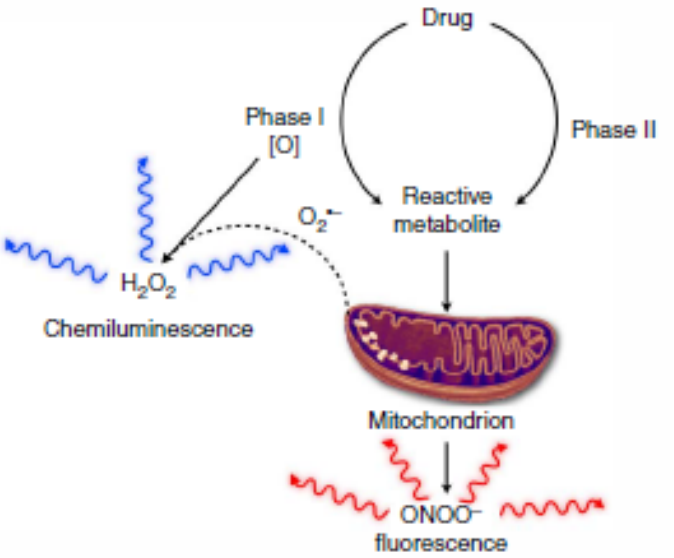

Design of CF-SPN for ROS & RNS detection

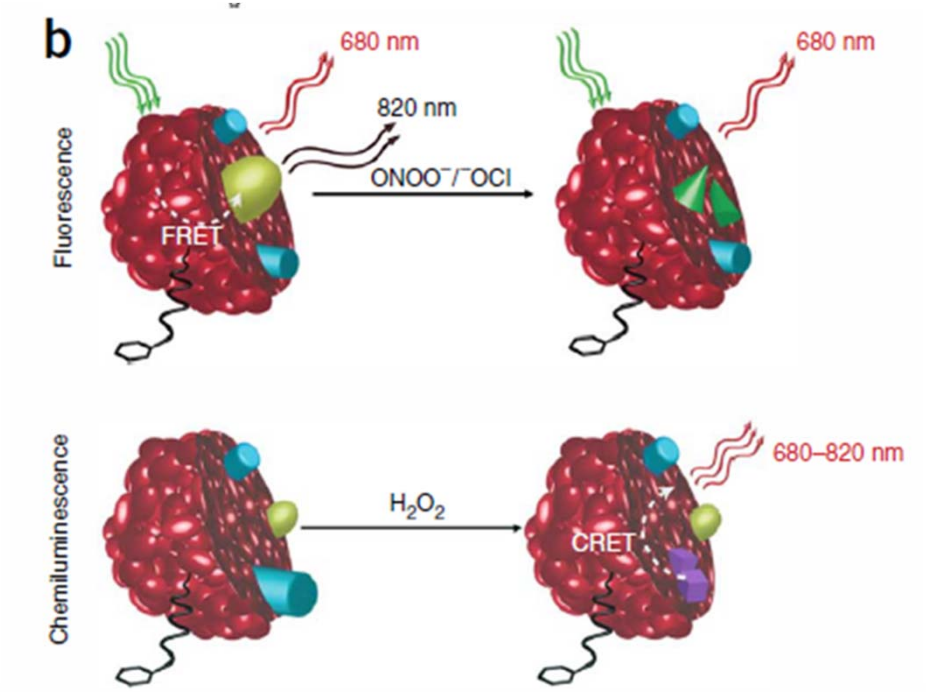

NIR fluorescent

a Semiconducting polymer core: PFODBT (CRET acceptor FRET donor)

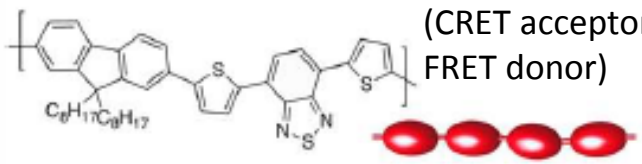

RNS-responsive dye: IR775S (FRET acceptor)

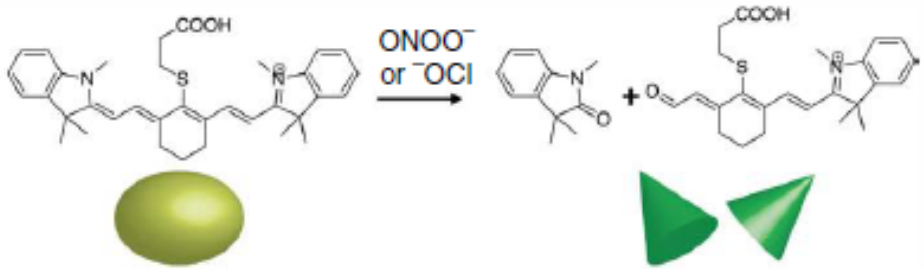

PEG-grafted poly(styrene) copolymer conjugated to galactose for hepatocyte targeting

Hepatocyte targeting group: PS-*g*-PEG-Gal

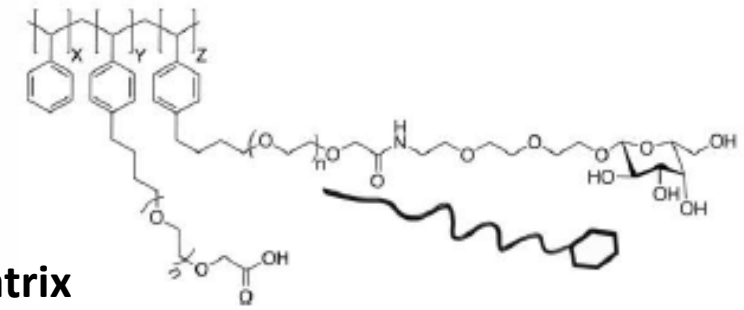

H_2O_2 -responsive chemiluminescent substrate: CPPO (CRET energy donor)

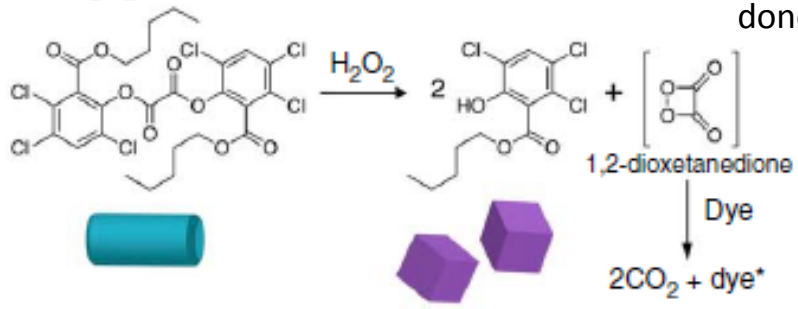

Matrix

In-vitro characterization of SPN

Dynamic light scattering

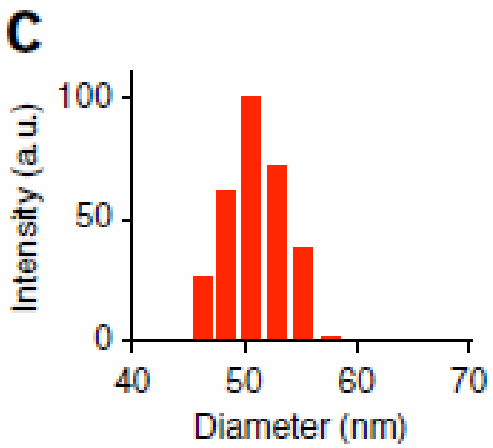

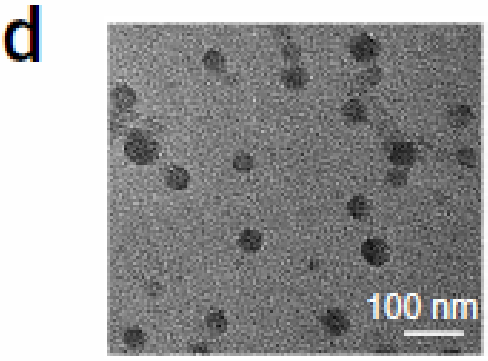

UV-visible absorption spectrum

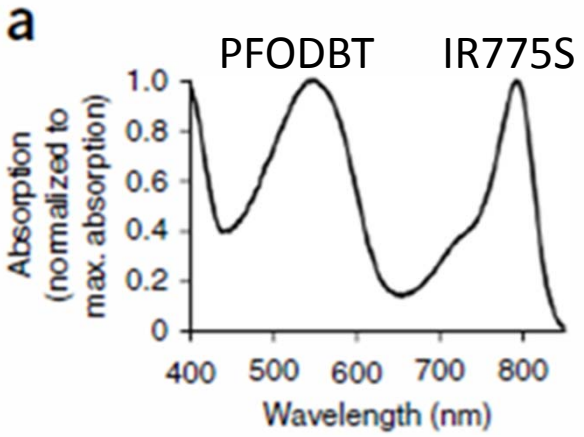

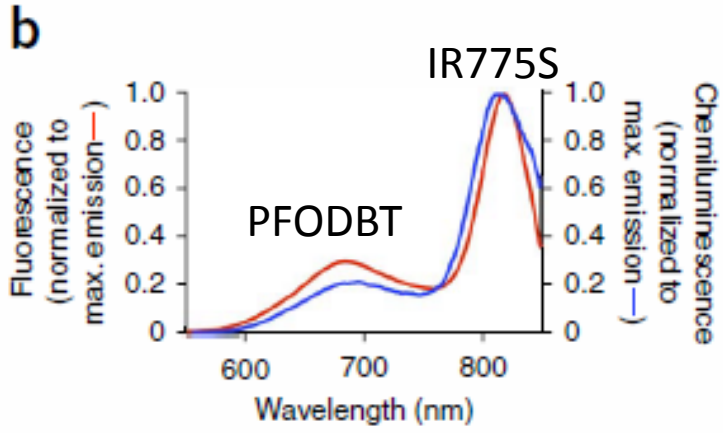

Transmission electron micrograph of CF-SPNs

Chemiluminescence was induced by the addition of 2 mM H_2O_2.

In-vitro characterization of SPN: specificity & sensitivity

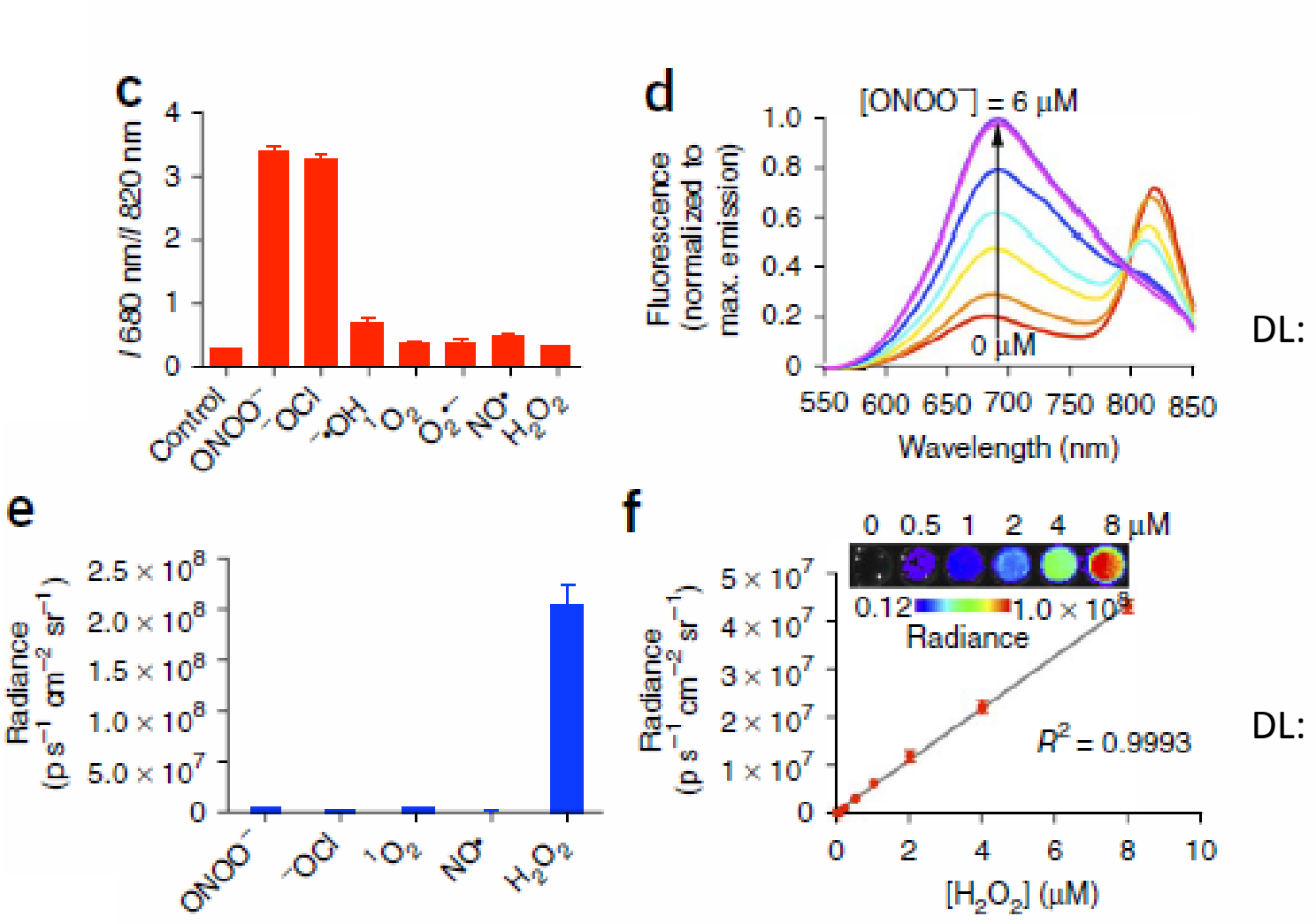

DL: 10nM

DL: 5nM

Longitudinal imaging of APAP hepatotoxicity in-vivo

analgesic and anti-pyretic
acetaminophen (APAP)

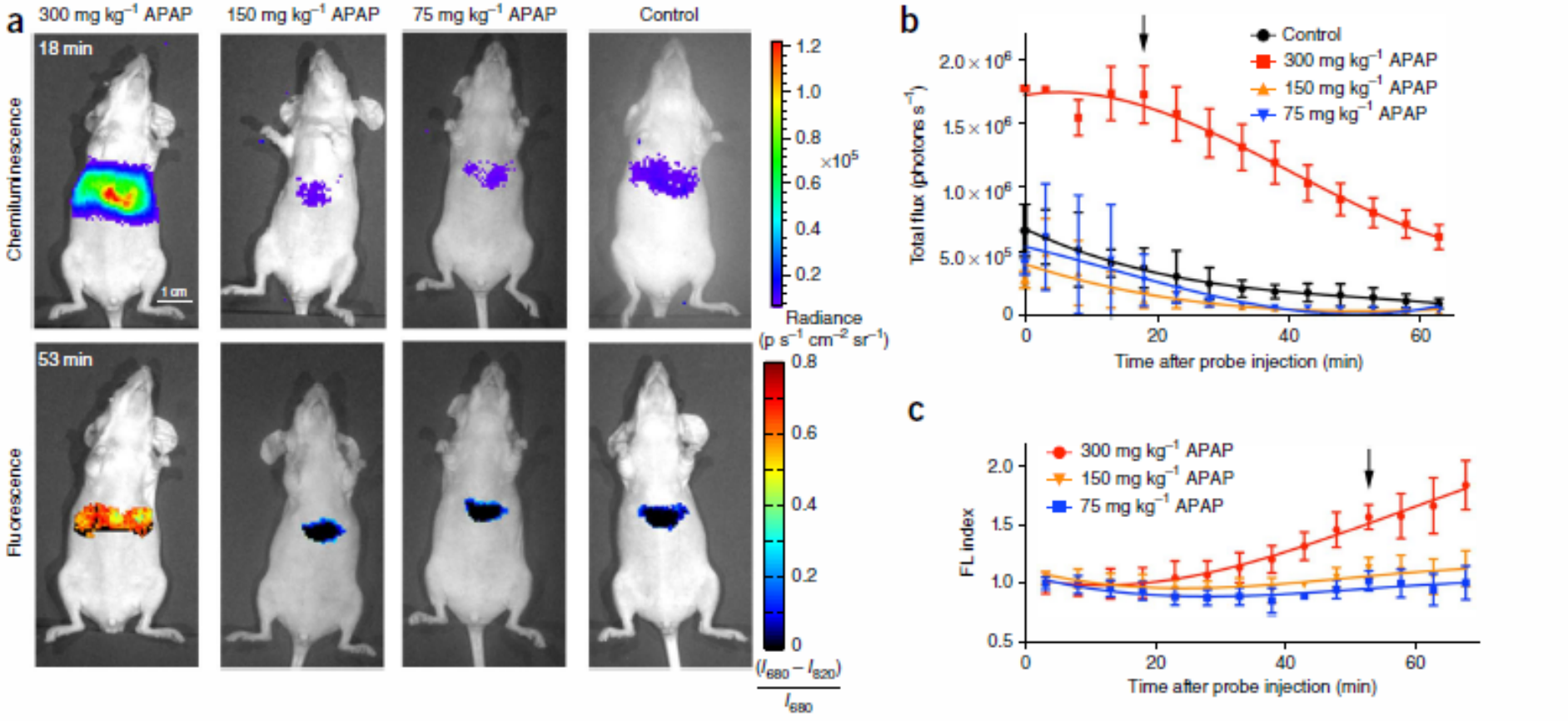

Figure 3 Real-time *in vivo* imaging of hepatotoxicity after APAP administration to mice. (**a**) Representative images of mice receiving APAP or saline (control) intraperitoneally, followed by CF-SPN (0.8 mg) intravenously. Chemiluminescence (top, imaged 18 min after CF-SPN administration) and fluorescence (bottom, imaged 53 min after CF-SPN administration) channels are shown ($n = 3$ mice per treatment group). (**b**,**c**) Emission intensities of the liver for chemiluminescence (**b**) and normalized fluorescence percentage difference (FL index) over time (**c**). Black arrows indicate the respective time points shown in **a**. Values are the mean ± s.d. for $n = 3$ mice. (**d**,**e**) Representative nitrotyrosine (top) and TUNEL (bottom) staining for liver 45 min (**d**) and 180 min (**e**) after drug administration ($n = 3$ mice per treatment group). Arrowheads mark positive cellular or nuclear staining, respectively. Scale bars, 10 μm.

Longitudinal imaging of (acetaminophen) APAP hepatotoxicity in-vivo

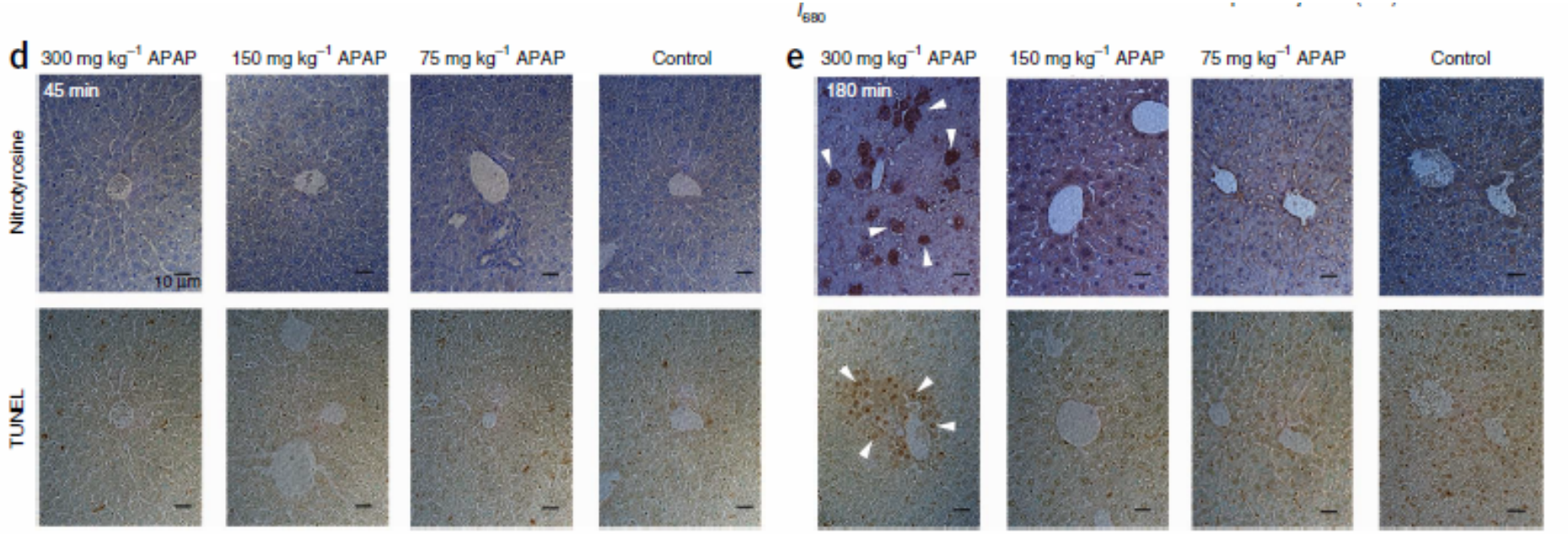

Figure 3 Real-time *in vivo* imaging of hepatotoxicity after APAP administration to mice. (**a**) Representative images of mice receiving APAP or saline (control) intraperitoneally, followed by CF-SPN (0.8 mg) intravenously. Chemiluminescence (top, imaged 18 min after CF-SPN administration) and fluorescence (bottom, imaged 53 min after CF-SPN administration) channels are shown ($n = 3$ mice per treatment group). (**b**,**c**) Emission intensities of the liver for chemiluminescence (**b**) and normalized fluorescence percentage difference (FL index) over time (**c**). Black arrows indicate the respective time points shown in **a**. Values are the mean ± s.d. for $n = 3$ mice. (**d**,**e**) Representative nitrotyrosine (top) and TUNEL (bottom) staining for liver 45 min (**d**) and 180 min (**e**) after drug administration ($n = 3$ mice per treatment group). Arrowheads mark positive cellular or nuclear staining, respectively. Scale bars, 10 µm.

Longitudinal imaging of APAP hepatotoxicity in-vivo

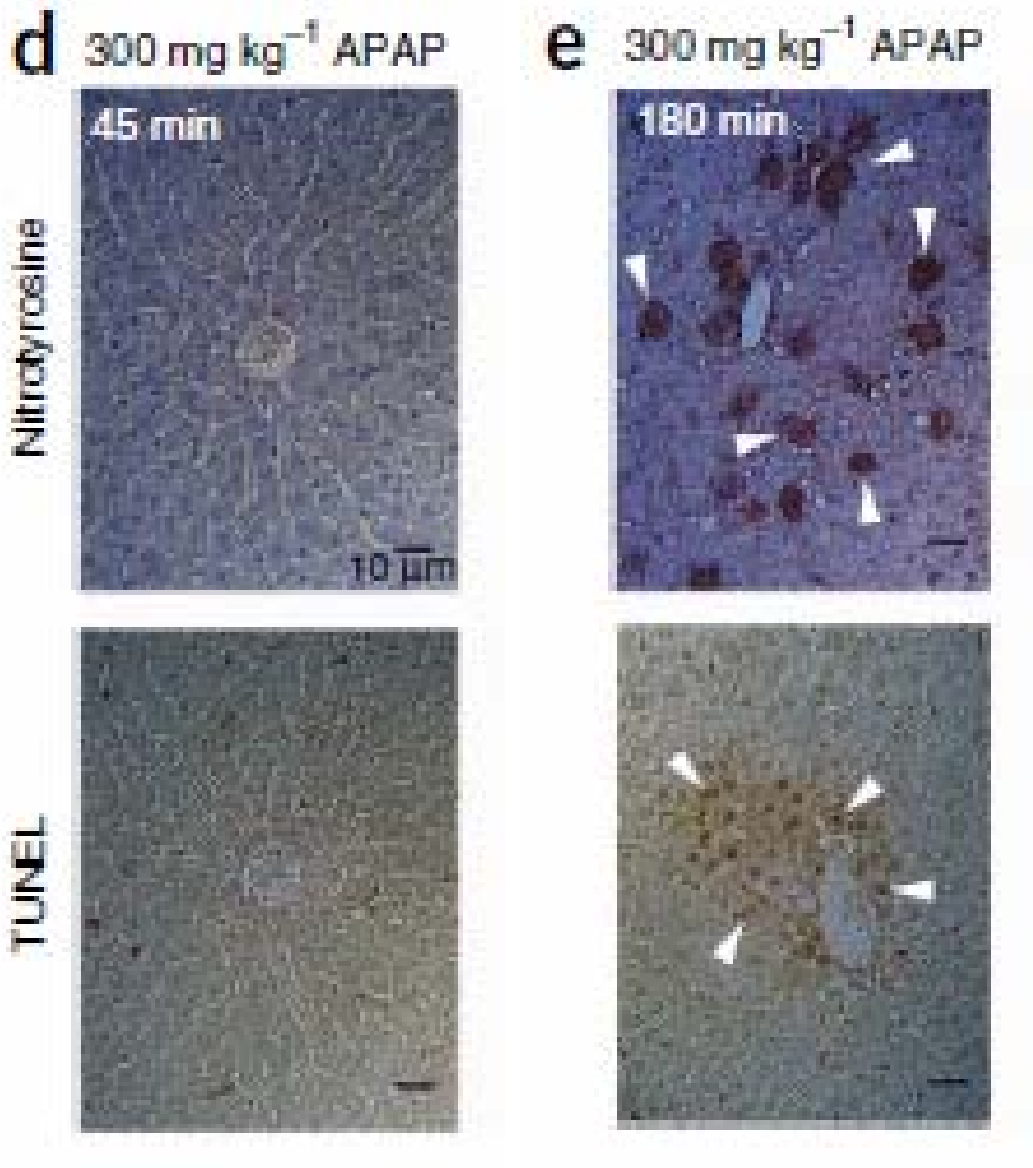

Longitudinal imaging of APAP hepatotoxicity in-vivo plus enzyme inhibitors and ROS scavengers

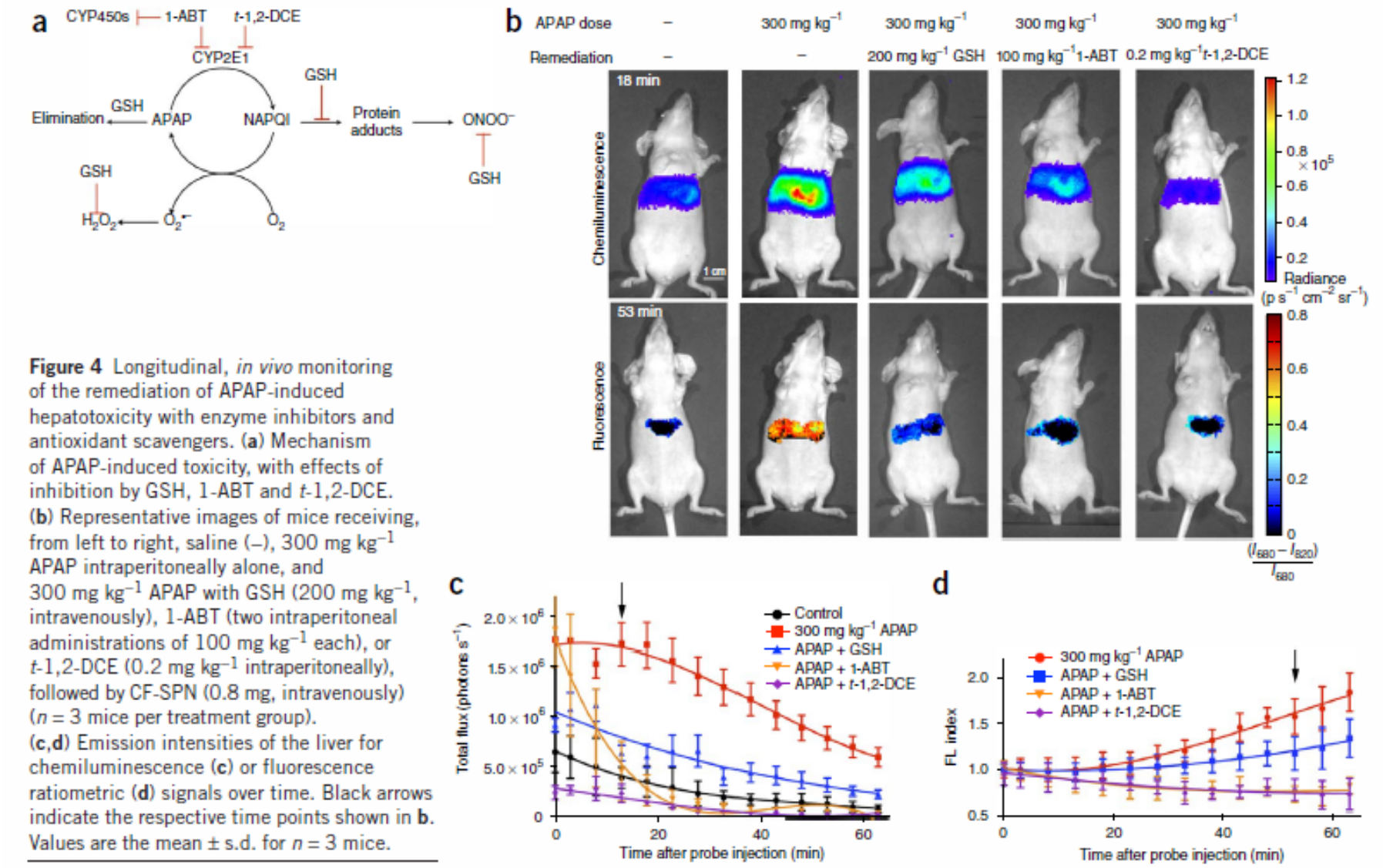

Figure 4 Longitudinal, *in vivo* monitoring of the remediation of APAP-induced hepatotoxicity with enzyme inhibitors and antioxidant scavengers. (**a**) Mechanism of APAP-induced toxicity, with effects of inhibition by GSH, 1-ABT and *t*-1,2-DCE. (**b**) Representative images of mice receiving, from left to right, saline (–), 300 mg kg^{-1} APAP intraperitoneally alone, and 300 mg kg^{-1} APAP with GSH (200 mg kg^{-1}, intravenously), 1-ABT (two intraperitoneal administrations of 100 mg kg^{-1} each), or *t*-1,2-DCE (0.2 mg kg^{-1} intraperitoneally), followed by CF-SPN (0.8 mg, intravenously) ($n = 3$ mice per treatment group). (**c**,**d**) Emission intensities of the liver for chemiluminescence (**c**) or fluorescence ratiometric (**d**) signals over time. Black arrows indicate the respective time points shown in **b**. Values are the mean ± s.d. for $n = 3$ mice.

Longitudinal imaging of isoniazid (INH) hepatotoxicity in-vivo

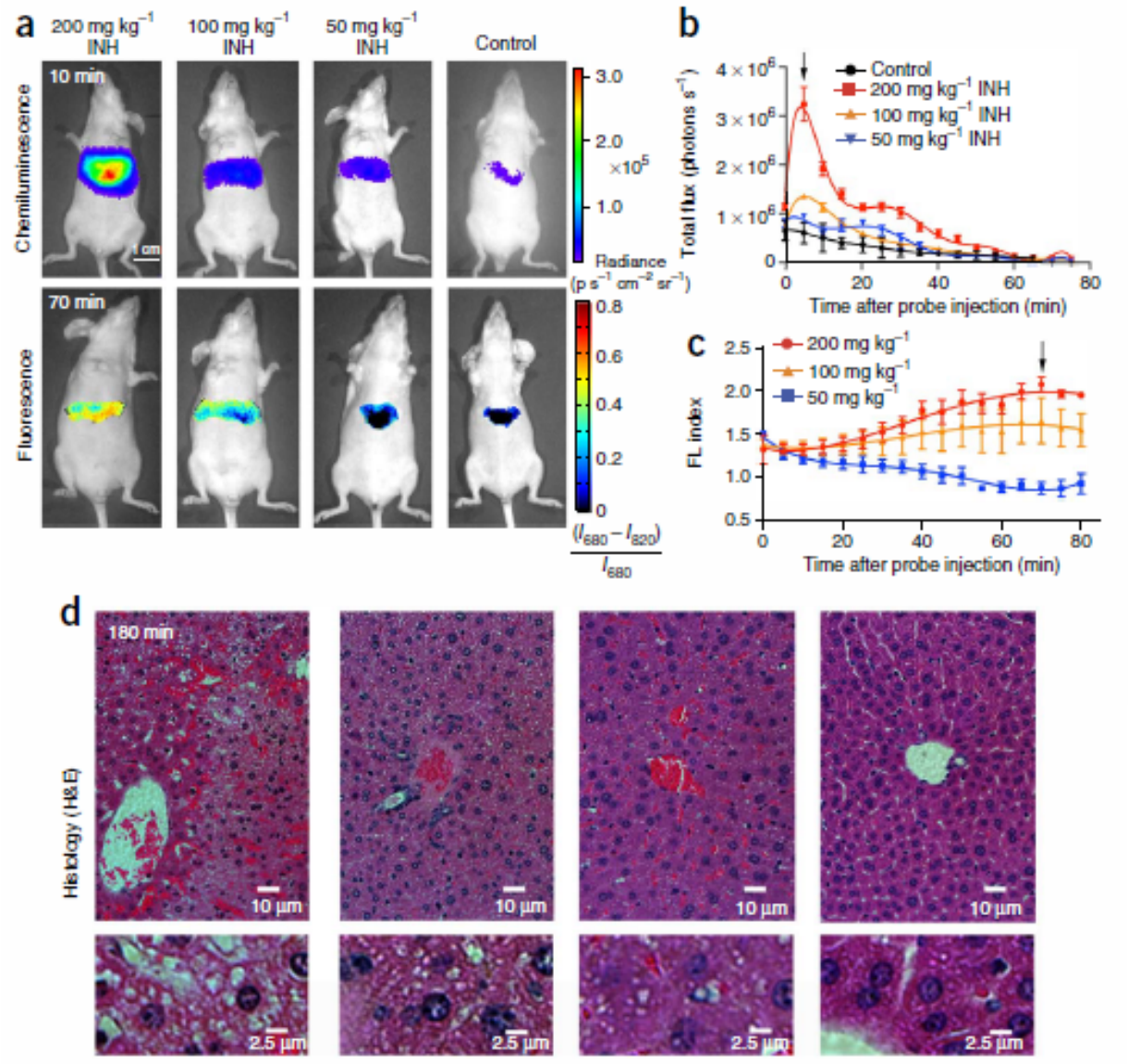

Figure 5 Real-time *in vivo* imaging of dose-dependent hepatotoxicity in mice after INH administration. (**a**) Representative images of mice that received INH or saline (control) intraperitoneally followed by CF-SPN (0.8 mg, intravenously) ($n = 3$ mice per treatment group). (**b**,**c**) Emission intensities of the liver for chemiluminescence (**b**) or fluorescence (**c**) ratiometric signals over time. Black arrows indicate the respective time points shown in **a**. Values are the mean ± s.d. for $n = 3$ mice. (**d**) Representative histology (hematoxylin and eosin staining (H&E)) of the liver of mice treated as in **a** is shown 180 min after drug administration (top), with corresponding image enlargements (bottom) ($n = 3$ mice per treatment group).

anti-tuberculosis agent
isoniazid (INH)

Summary on FRET-CRET SPNs

- Rapid, real-time in vivo imaging probes for drug-induced ROS and RNS and direct evaluation of acute hepatotoxicity.
- Simultaneous and differential detection of RNS and ROS using two optically independent channels by combining fluorescence resonance energy transfer (FRET) and chemiluminescence resonance energy transfer (CRET)

- Imaging of drug-induced hepatotoxicity and its remediation longitudinally in mice after systemic challenge with acetaminophen or isoniazid→ dose-dependent ROS and RNS activity in the liver detected within minutes of drug challenge, preceded histological changes, protein nitration and DNA double-strand-break induction.

Advantages of semiconducting polymers for biomedical imaging

- large mass extinction coefficients that result in efficient fluorescence
- excellent acute and subacute polymer biocompatibility equivalent to that of FDA-approved poly(lactate-co-glycolate)
- excellent photostability

- Both quantum dots and small-molecule fluorophores undergo chemical degradation by ROS and RNS, including H_2O_2, $ONOO^-$ and ^-OCl, whereas SPNs are resistant to such oxidative chemical bleaching effects

Bioactivation of drugs

Bioactivation through drug metabolism is frequently suspected as an initiating event in many drug toxicities.

The CYP450 and peroxidase enzyme systems are generally considered the most important groups of enzymes involved in bioactivation, producing either electrophilic or radical metabolites.

Structural alerts are aromatic systems with electron-donating substituents and some five-membered heterocycles. Metabolism of these groups can lead to chemically reactive electrophiles.

Walsh et al. Annu. Rev. Pharmacol. Toxicol. 2011

Bioactivation of drugs: risk & drug design

Enzymes mechanisms and formation of chemically reactive species

Table 1 Structural alerts, types of reactive species produced, and the enzyme system most commonly responsible

Functional group	Reactive species	Enzyme system
Nitro aromatics	Radical	CYP450/reductase
Anilines	Electrophiles	CYP450, peroxidases
Activated aromatics	Electrophiles, radicals	CYP450, peroxidases
Propionic acids	Electrophiles	Glucuronyl transferase
Thiophenes	Electrophiles	CYP450
Furans	Electrophiles	CYP450
Formamides	Electrophiles	CYP450
3-Alkyl indoles	Electrophiles	CYP450
Thioureas	Electrophiles	CYP450
Thioamides	Electrophiles	CYP450
Thiazolidinones	Electrophiles	CYP450
Cyclopropyl amines	Radicals	CYP450
Hydrazines	Radicals	CYP450
Acetylenes	Electrophiles	CYP450
Sulfonylureas	Electrophiles	CYP450

Walsh et al. Annu. Rev. Pharmacol. Toxicol. 2011

Strategies to minimize bioactivation risk

A wide range of functional groups are known to undergo bioactivation. These groups cannot always be avoided in drug design.

Bioactivation risk can be avoided or minimized by

(a) replacing the suspect functional group

(b) blocking metabolism

(c) making metabolism less favorable

(d) switching to metabolic soft spots

Walsh et al. Annu. Rev. Pharmacol. Toxicol. 2011

nature COMMUNICATIONS

ARTICLE

Received 19 Apr 2012 | Accepted 10 Oct 2012 | Published 13 Nov 2012

DOI: 10.1038/ncomms2197

Self-luminescing BRET-FRET near-infrared dots for *in vivo* lymph-node mapping and tumour imaging

Liqin Xiong[1,†], Adam J. Shuhendler[1] & Jianghong Rao[1]

Strong autofluorescence from living tissues, and the scattering and absorption of short-wavelength light in living tissues, significantly reduce sensitivity of *in vivo* fluorescence imaging. These issues can be tackled by using imaging probes that emit in the near-infrared wavelength range. Here we describe self-luminescing near-infrared-emitting nanoparticles employing an energy transfer relay that integrates bioluminescence resonance energy transfer and fluorescence resonance energy transfer, enabling *in vivo* near-infrared imaging without external light excitation. Nanoparticles were 30–40 nm in diameter, contained no toxic metals, exhibited long circulation time and high serum stability, and produced strong near-infrared emission. Using these nanoparticles, we successfully imaged lymphatic networks and vasculature of xenografted tumours in living mice. The self-luminescing feature provided excellent tumour-to-background ratio (>100) for imaging very small tumours (2–3 mm in diameter). Our results demonstrate that these new nanoparticles are well suited to *in vivo* imaging applications such as lymph-node mapping and cancer imaging.

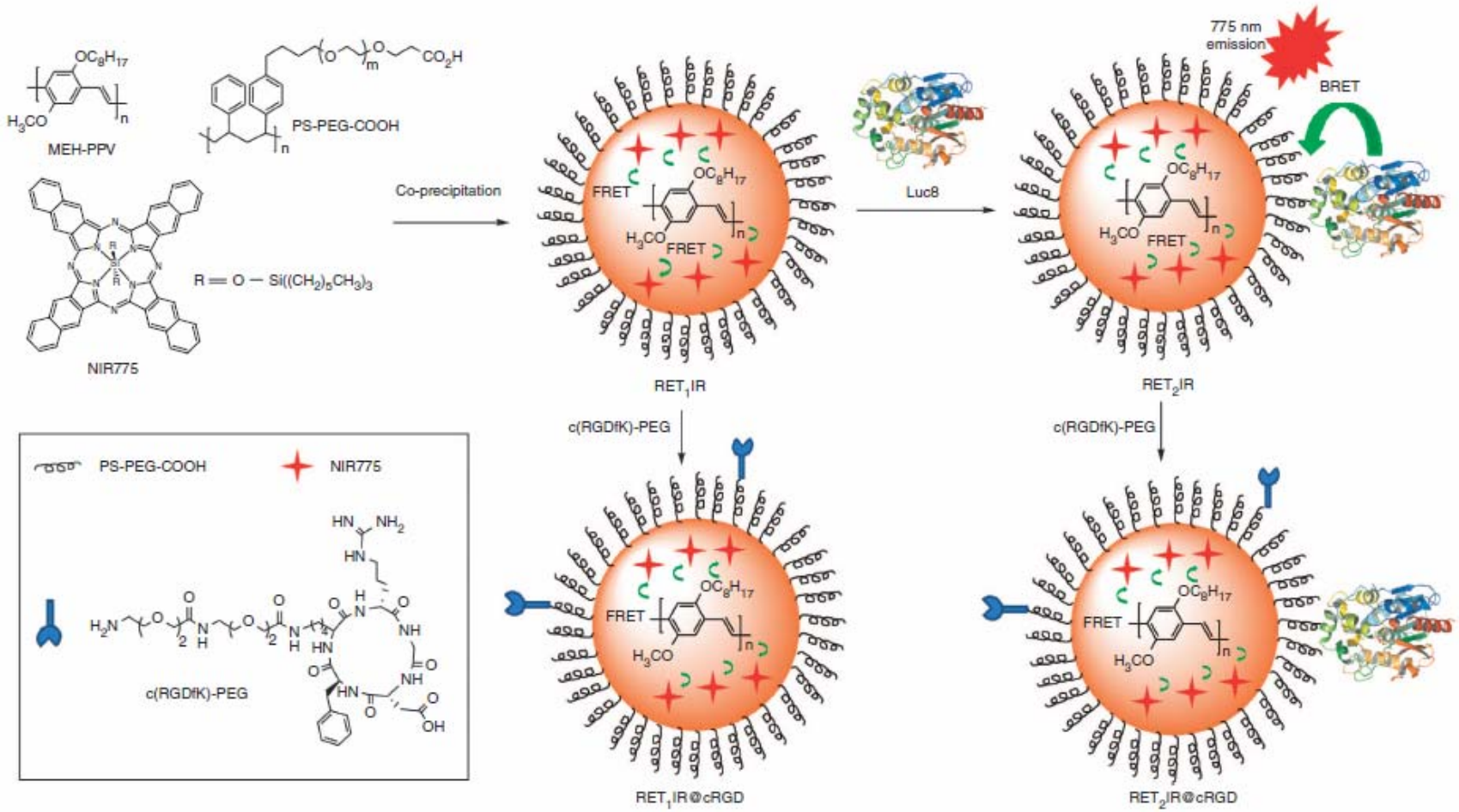

Figure 1 | Schematic of self-luminescing BRET-FRET NIR polymer nanoparticles. The biochemical energy generated from the Luc8-catalysed oxidation of coelenterazine transfers initially to the MEH-PPV polymer and is then relayed to doped NIR775 dye to produce NIR emission. An amphiphilic polymer, PS-PEG-COOH, coats the nanoparticle to improve water solubility and biocompatibility. Tumour targeting ligands such as cyclic RGD peptides are conjugated to the nanoparticle surface for *in vivo* cancer imaging.

Figure 2 | *In vitro* characterization of RETIR nanoparticles. (**a**) Ultraviolet-vis absorption and fluorescence emission spectra of **RET$_2$IR** NPs in PBS buffer. (**b**) Bioluminescence emission spectrum of **RET$_2$IR** NPs in PBS buffer. (**c**) Representative TEM image of **RET$_2$IR** NPs. Scale bar = 200 nm. (**d**) Dynamic light scattering (DLS) measurement of four indicated NP formulations in water by lognormal size distribution. (**e**) Gel electrophoresis (0.5% agarose) analysis of RET NPs in tris-borate-EDTA (TBE) buffer: **RET$_1$IR** (lane 1), **RET$_1$IR@cRGD** (lane 2), **RET$_2$IR** (lane 3), **RET$_2$IR@cRGD** (lane 4). (**f**) Bioluminescent and NIR fluorescent intensity of **RET$_2$IR** NPs (1 μg) in mouse serum at 37 °C from 0 to 24 h. Data points represent mean ± s.d. (n = 3). (**g**) The NIR fluorescence signals of blood samples of mice injected with **RET$_1$IR** NPs (~20 μg) from 5 min to 24 h. Data represent mean ± s.d. (n = 4). (**h**) Viability values (%) of U87MG cells estimated by MTT assay versus incubation concentrations of **RET$_1$IR** NPs. Data represent mean + s.d. (n = 3).

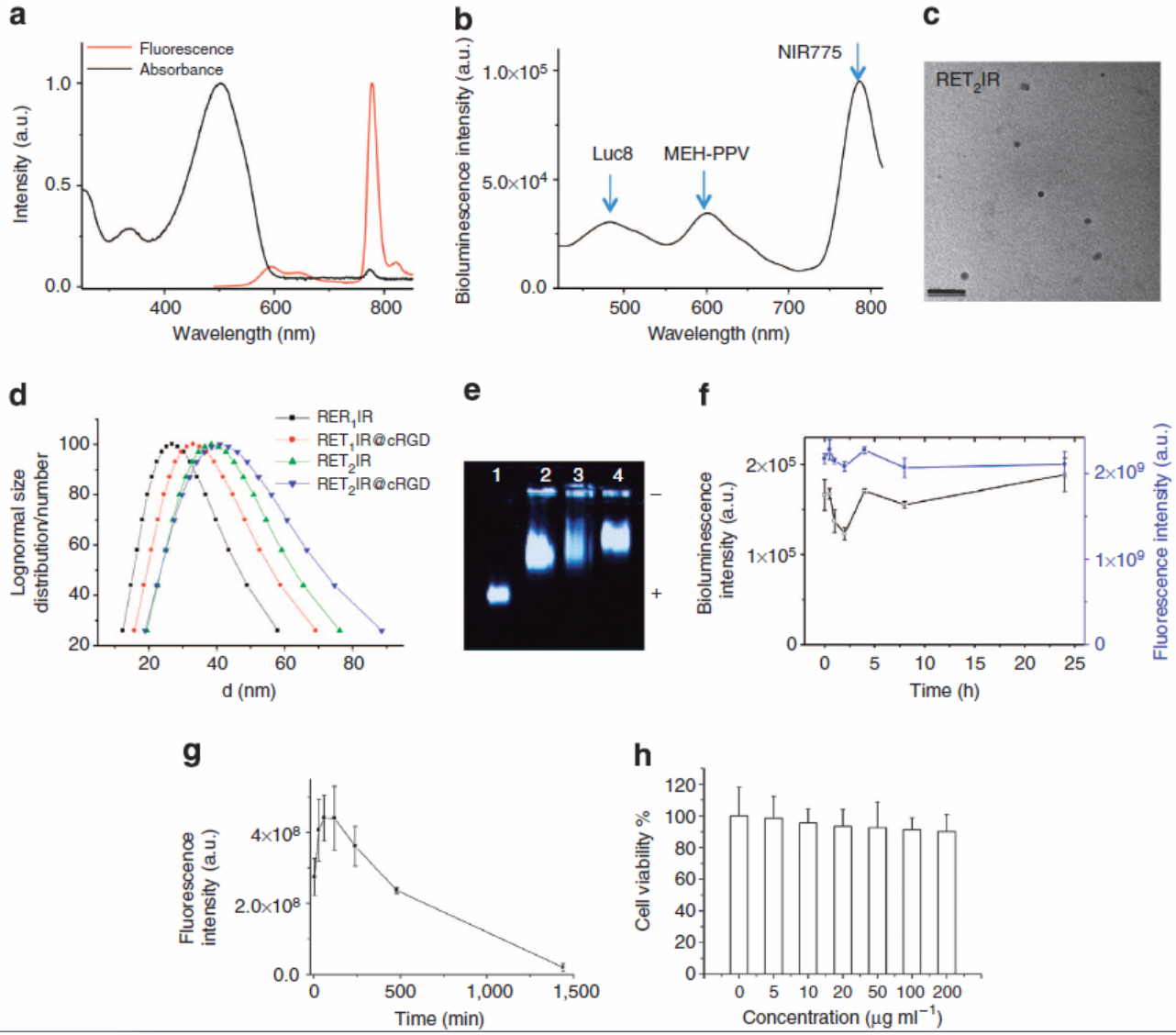

Figure 3 | Fluorescence and bioluminescence imaging of lymph nodes in mice. (**a**) Fluorescence imaging of a mouse following and necropsy 24 h after the tail-vein injection of **RET$_1$IR** NPs (~20 μg). Superficial skin was removed before imaging but peritoneum was left intact. Autofluorescence is coded in green and NPs signal in red; AX, axillary lymph node; IN, inguinal lymph node; L, left; LT, lateral thoracic lymph node; NL, neck lymph nodes; R, right. (**b**) Fluorescence image of lymph nodes excised from the mouse in (**a**): 1–4, NL; 5, AX (left); 6, LT (left); 7, LT (right); 8, AX (right); 9, IN (left), 10 IN (right). (**c**) Bioluminescence and (**d**) fluorescence imaging of lymphatic basins in a mouse 10 min after the injection of **RET$_2$IR** NPs (~2 μg) intradermally in the forepaws. (**e**) Bioluminescence imaging of lymphatic basins in a mouse with injection of **RET$_2$IR** NPs (~2 μg) intradermally in the forepaws. All bioluminescence images were acquired with 10 s exposure time; L, left; LU, lumbar lymph node; PO, popliteal lymph node; R, right.

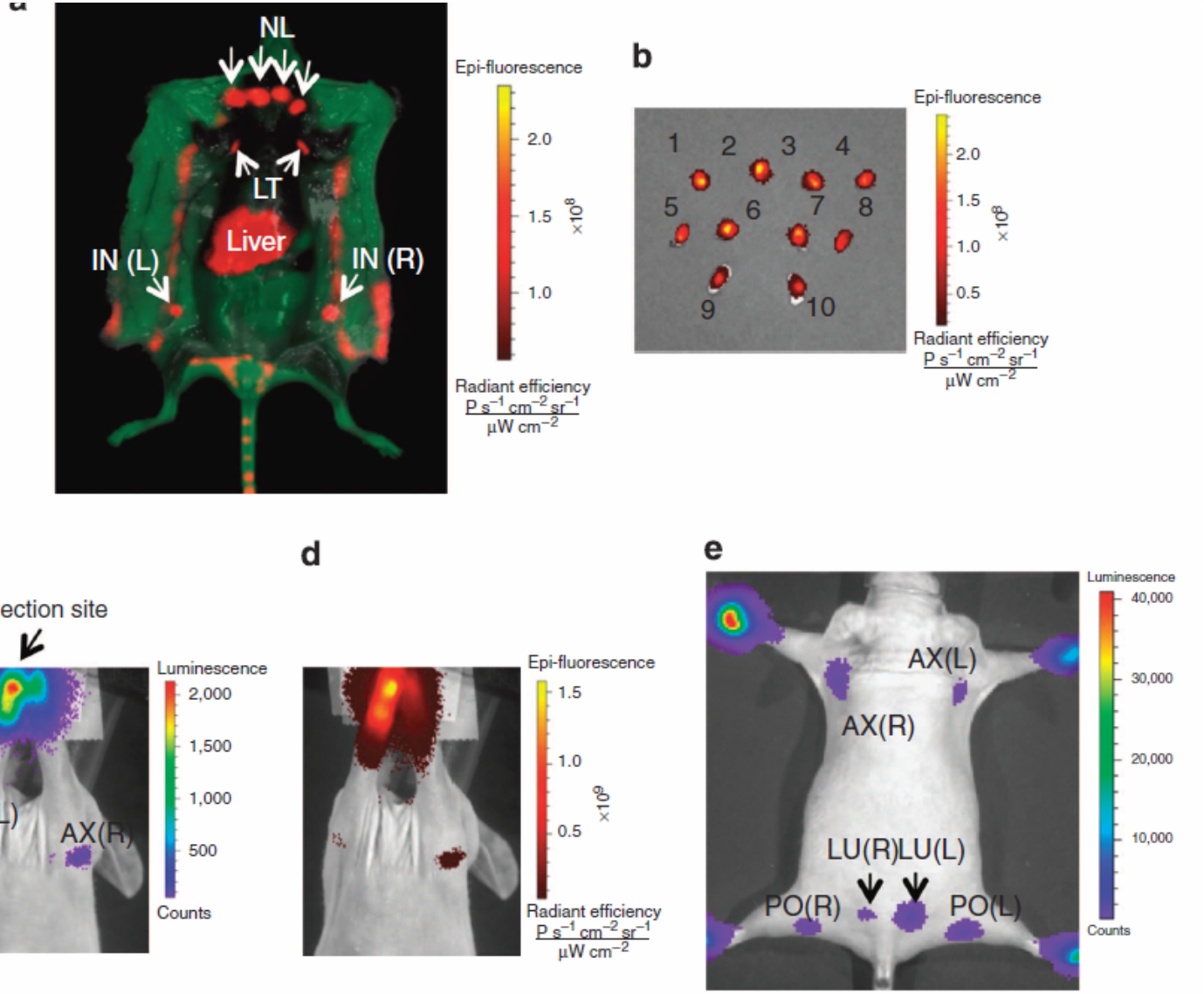

Figure 4 | Fluorescence imaging of U87MG cells *in vitro* and *in vivo* with RET_1IR@cRGD NPs. (**a**–**c**) Live imaging of U87MG cells *in vitro* incubated with **RET_1IR@cRGD** NPs (4 μg) for (**a**) 2.5 h and (**b**) 24 h, or (**c**) incubated with **RET_1IR** NPs without cRGD for 24 h. Scale bar: 20 μm; excitation: 480/30 nm, dichroic beamsplitter: Q570LP, emission: D755/40M; objective: × 20; acquisition time: 1 s. (**d**,**e**) Time-dependent fluorescence imaging of U87MG tumour-bearing mouse (tumours are indicated by white arrows and circles, and are 4 mm in diameter) injected with (**d**) **RET_1IR@cRGD** or (**e**) **RET_1IR** NPs (each at ~50 μg) after 5 min, 2, 24 and 48 h. Autofluorescence is coded in green and the unmixed polymer nanoparticle signal in red. (**f**) Fluorescence spectra of tissue autofluorescence (green) and the unmixed nanoparticle signal (red) in a living mouse. (**g**) Region of interest (ROI) analysis of fluorescence intensity of tumour over background of mice in (**d**) and (**e**). Using one-tailed paired Student's *t*-test ($n = 3$ mice injected with **RET_1IR@cRGD**), $P < 0.05$ at 24 h. (**h**,**i**) NIR fluorescence imaging of urine samples (**h**) collected 48 h after injection from mouse in (**d**), and (**i**) from a mouse without any nanoparticle injection.

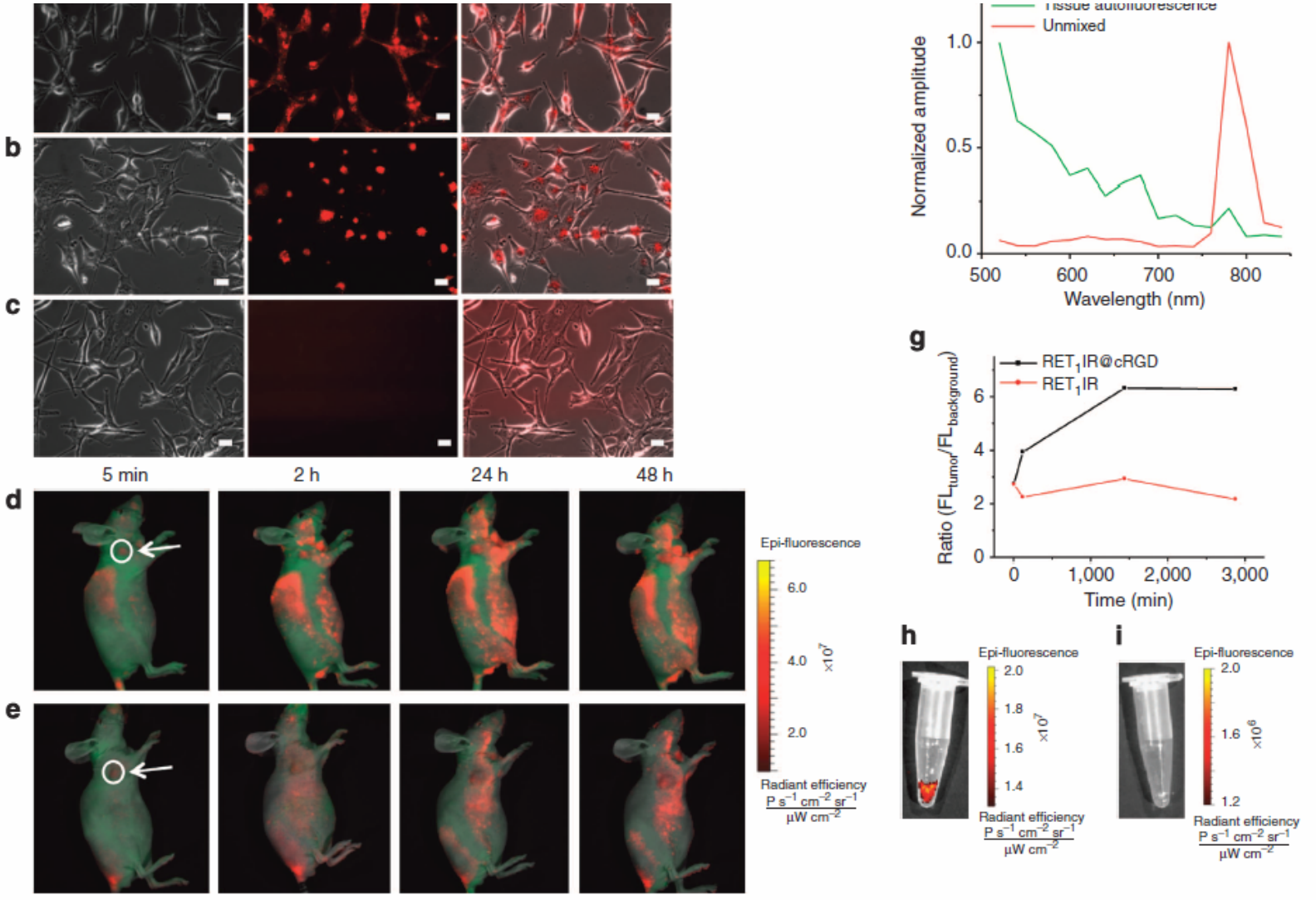

Figure 5 | *In vivo* imaging of U87MG tumours in mice with RET_2IR@cRGD. (**a**,**b**) Time-dependent (**a**) *in vivo* bioluminescence and (**b**) fluorescence imaging of U87MG tumour-bearing mouse (indicated by a red arrow and circle; tumour size was about 5 mm in diameter) injected with **RET_2IR@cRGD** NPs (~50 μg). Acquisition time for images in (**a**) from left to right: 15 s (5 min), 15 s (2 h), 1 min (24 h), 1 min (48 h) and 3 min (48 h). (**c**) ROI analysis of the bioluminescence and fluorescence intensity between tumour and background of mice in (**a**) and (**b**). Using one-tailed paired Student's *t*-test ($n=3$), $P<0.00002$ at 5 min, and 2 h, $P<0.04$ at 24 h and $P>0.05$ at 48 h. (**d**) *In vivo* bioluminescence imaging of a mouse with a small tumour of 2 mm in diameter, as indicated by a red arrow, 2 h after tail vein injection of **RET_2IR@cRGD**. (**e**) NIR fluorescence imaging of urine samples collected 48 h after injection from mice in (**a**). Data points represent mean ± s.d. ($n=4$) (**f–i**) Histological imaging of frozen U87MG tumour slices from mouse in (**a**): (**f**) bright field, (**g**) NIR fluorescence (excitation filter: 480/30 nm, dichroic beamsplitter: Q570LP, emission filter: D755/40M, acquisition: 1 s), (**h**) Alexa Fluor 488 anti-mouse CD31 (excitation: 480/30 nm, dichroic beamsplitter: 505DCLP, emission: D535/40 nm, acquisition time: 200 ms) and (**i**) overlay of images in (**g**) and (**h**). Scale bar: 20 μm, objective: ×20.